

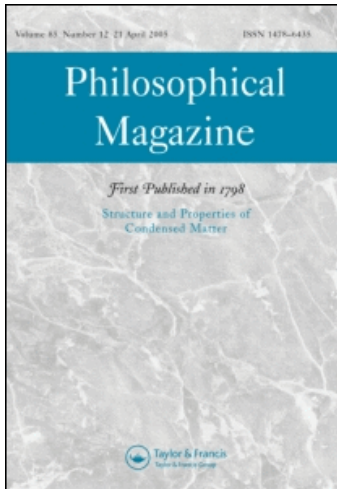
This article was downloaded by: [NIST National Institutes of Standards & Technology]

On: 2 September 2009

Access details: Access Details: [subscription number 910161337]

Publisher Taylor & Francis

Informa Ltd Registered in England and Wales Registered Number: 1072954 Registered office: Mortimer House, 37-41 Mortimer Street, London W1T 3JH, UK



Philosophical Magazine

Publication details, including instructions for authors and subscription information:

<http://www.informaworld.com/smpp/title-content=t713695589>

Fundamental relationships between deformation-induced surface roughness, critical strain localisation and failure in AA5754-O

Mark R. Stoudt ^a; Joseph B. Hubbard ^a

^a Materials Science and Engineering Laboratory, National Institute of Standards and Technology, Gaithersburg 20899, MD, USA

Online Publication Date: 01 September 2009

To cite this Article Stoudt, Mark R. and Hubbard, Joseph B. (2009) 'Fundamental relationships between deformation-induced surface roughness, critical strain localisation and failure in AA5754-O', *Philosophical Magazine*, 89:27, 2403 — 2425

To link to this Article: DOI: 10.1080/14786430903120343

URL: <http://dx.doi.org/10.1080/14786430903120343>

PLEASE SCROLL DOWN FOR ARTICLE

Full terms and conditions of use: <http://www.informaworld.com/terms-and-conditions-of-access.pdf>

This article may be used for research, teaching and private study purposes. Any substantial or systematic reproduction, re-distribution, re-selling, loan or sub-licensing, systematic supply or distribution in any form to anyone is expressly forbidden.

The publisher does not give any warranty express or implied or make any representation that the contents will be complete or accurate or up to date. The accuracy of any instructions, formulae and drug doses should be independently verified with primary sources. The publisher shall not be liable for any loss, actions, claims, proceedings, demand or costs or damages whatsoever or howsoever caused arising directly or indirectly in connection with or arising out of the use of this material.

Fundamental relationships between deformation-induced surface roughness, critical strain localisation and failure in AA5754-O

Mark R. Stoudt* and Joseph B. Hubbard

Materials Science and Engineering Laboratory, National Institute of Standards and Technology, Gaithersburg 20899, MD, USA

(Received 6 March 2009; final version received 7 June 2009)

This research employs two approaches to characterise the apparent structure observed in localised strain maps constructed from surface topography data acquired from AA5754-O sheet stock that was deformed in three in-plane stretching modes. The first uses a conventional two-point autocorrelation function (ACF), while the second uses the combination of the eigenvalue spectrum associated with each map and information theory. The results from the ACF analysis are inconclusive, implying that this technique lacks the sensitivity necessary to quantify the relationships between multi-point clustering and strain localisation. The information theory-based approach reveals that the relative spectral entropy increases monotonically, attains a maximum and then decreases sharply to the failure strain. This behaviour occurs in all three strain modes and results from two competing processes: one where the formation of structure is favourable and one where it is not. The crossover point is a clear indicator of the onset of critical strain localisation and, therefore, can be regarded as a precursor to failure because once the dominant process shifts, additional strain results in the precipitate formation of a critical strain localisation event.

Keywords: information theory methods; aluminium alloys; mechanical behaviour; plastic deformation; polycrystalline metals; sheet metal forming; topological analysis

1. Introduction

The inability to reliably model the evolution of the surface inhomogeneities produced during sheet metal forming is a significant obstacle impeding the widespread incorporation of new alloys designed to reduce gross vehicle weight and increase overall vehicle fuel economy. The macroscopic deformation in a typical metal stamping occurs through a complex combination of strain modes (e.g. biaxial, uniaxial, plane strain). Since each strain mode imposes distinctly different constraints on the material flow during stretch forming, the strain mode strongly influences both the magnitudes of the limiting strains achievable through stretch forming, and the overall character of the deformed surface. The topographies shown in Figure 1 provide an example of how the constraints on material flow result in considerably

*Corresponding author. Email: stoudt@nist.gov

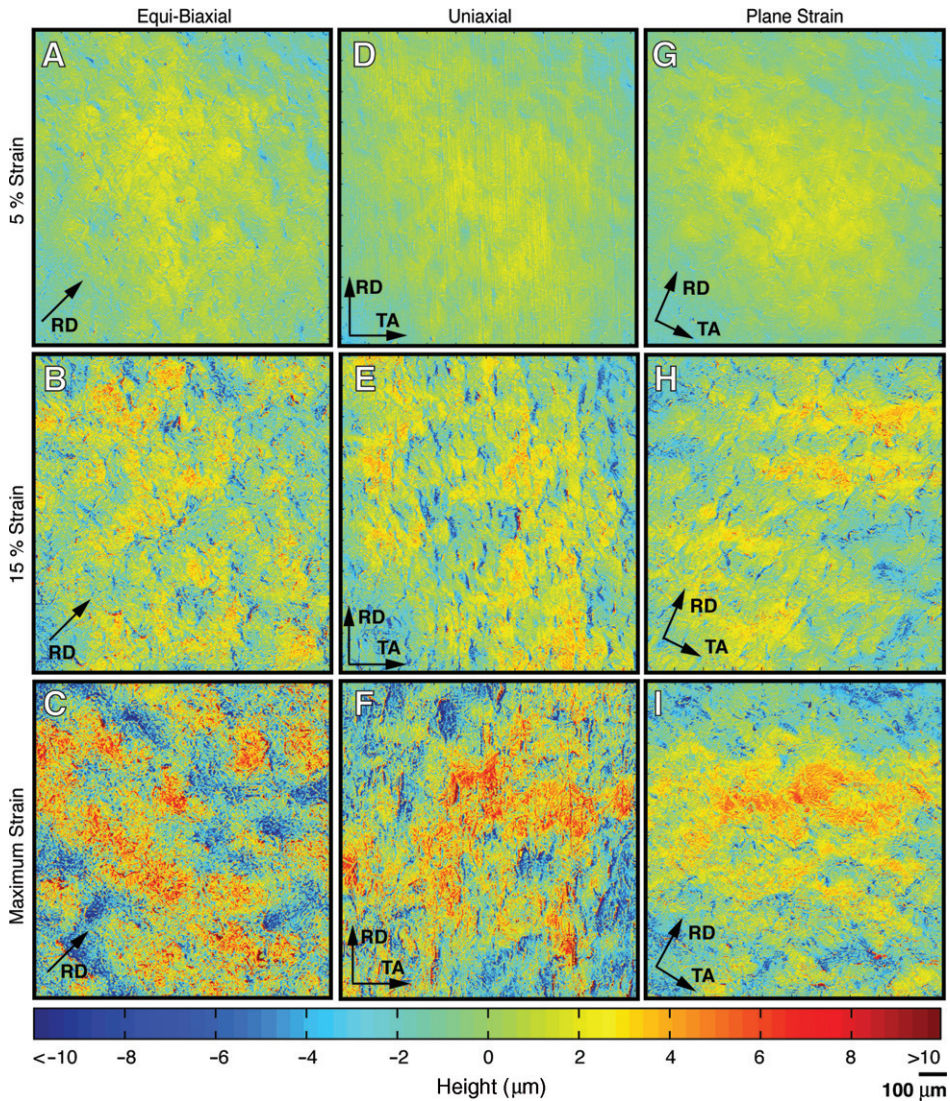


Figure 1. (Colour online). A representative set of scanning laser confocal topographies showing the surface structure of AA5754-O at three strain levels in three strain modes. Images A, B and C are in equi-biaxial strain, D, E, and F are in uniaxial strain and G, H, and I are in plane strain. Images A, D, and G show the surfaces after 5% nominal true strain, B, E, and H show the surfaces after 10% nominal true strain and C, F, and I show the surfaces at the maximum uniform strain.

different surface morphologies for the same level of modal plastic strain. The problem arises from the fact that a combination of strain modes normally produces failure at a lower strain compared to that achieved in a single strain mode. Owing to the complexity of the automotive component shapes produced with metal stamping, the limiting strains for these components are generally determined through

numerical simulations specifically designed to predict the onset of critical strain localisation (i.e. one that is a direct precursor to failure such as the formation of cracks or splits, necks, etc.). Clearly, the accuracy of these models is heavily dependent on the quality of the materials data, and a correct prediction of the forming behaviour requires that the surfaces produced by each component of the macroscopic strain be properly identified and correctly characterised. Such characterisations are expensive and complicated processes that require numerous high-resolution measurements of the surface morphology produced by each strain mode [1].

The incorporation of revised plasticity and kinematic hardening models, as well as the results from numerous studies of the influence of various material parameters, such as grain size, grain orientation effects, surface roughening effects and other damage mechanisms, on strain localisation have greatly enhanced the reliability of the numerical models used to predict the limiting strains [2–9]. Despite all the improvements, inconsistencies still exist between the mechanical behaviour predicted numerically and that observed experimentally. This creates a situation where the numerical models often correctly indicate the general trends, but fail to consistently predict the actual strains at which localisation occurs [10].

This paper is one in a series documenting analyses of strain localisation behaviour in commercial aluminium sheet [11–13]. The inspiration for this research is derived from the work of Frost and Ashby [14], and others [15,16], in that changes in the microstructure or, in this case, surface morphology, can be ‘mapped’ with respect to the level of plastic deformation. Previously [11], rigorous matrix-based statistical analysis methods were developed and integrated with high-resolution topographical imaging (Figure 1) to assess how plastic deformation and microstructure evolution influence strain localisation in aluminium sheet deformed in three in-plane strain modes. A key component of this approach involves extending the peak-to-valley surface roughness (Rt) to a matrix form, which is done for three reasons: (1) the magnitudes of the local surface extremes will change with strain to the point where they reach a value that directly reflects the onset of critical strain localisation, (2) the Rt parameter is highly sensitive to those localised changes and it is acquired through a straightforward calculation, and (3) the Rt parameter is based on a simple sum of two values, so it can be easily determined between any two nodes within a particular region in a finite element simulation, allowing for direct integration of changes in the intensity of the local surface conditions into formability models. The result is a series of local intensity maps consisting of discretised arrays of Rt ‘cells’ constructed from the raw topographic data (an example is shown in Figure 2). Each cell accentuates the height disparities between topographical features, enabling a direct three-dimensional quantification of the microstructural conditions that promote critical strain localisation. So far, this study has established that (1) the morphological conditions that promote strain localisation can be assessed directly through topographic analysis, (2) an accurate and straightforward probabilistic expression that captures the subtle changes produced in the morphology can be developed, and (3) strain localisation is controlled by a stochastic process that can be reliably predicted with Weibull statistical methods.

The objective of the present investigation is to ascertain whether critical strain localisation requires the formation of ‘structure’ within the Rt maps (i.e. several Rt

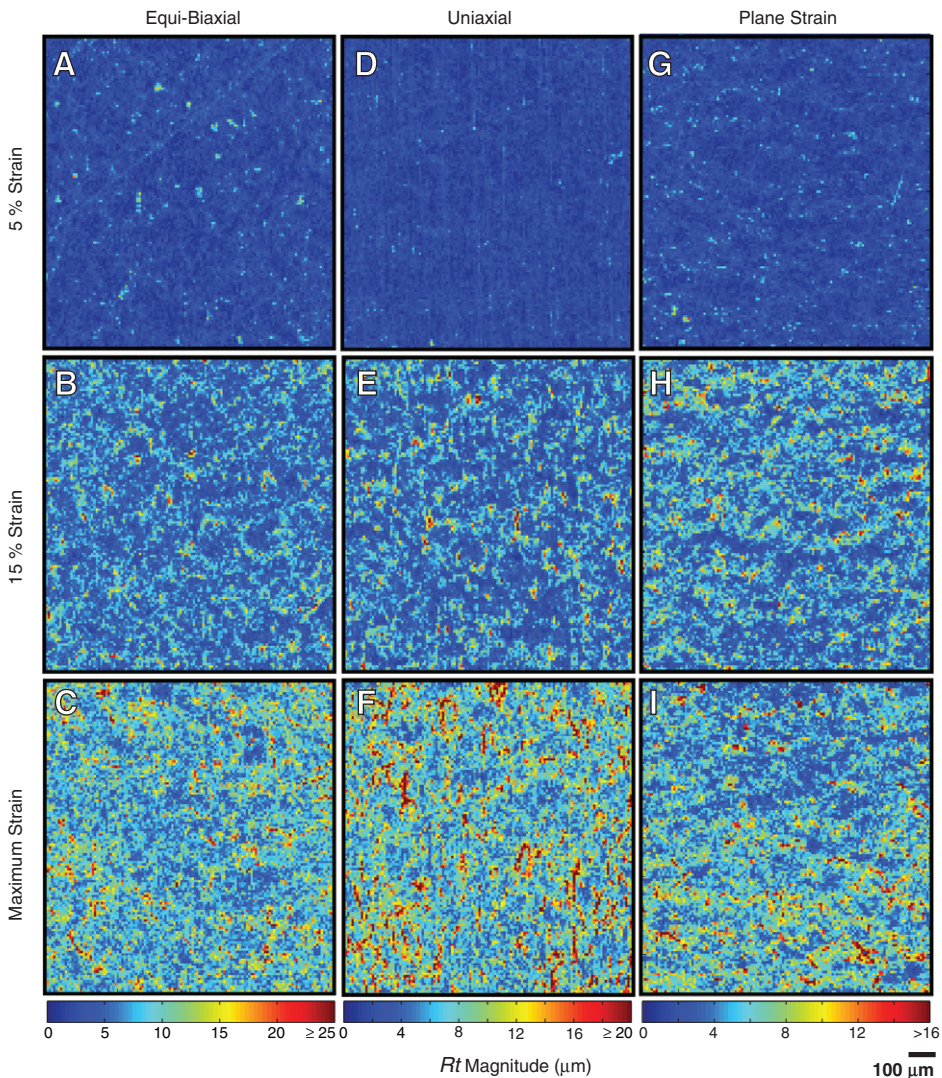


Figure 2. (Colour online). The set of localisation maps constructed from the peak-to-valley distance (Rt) data calculated for the topographies shown in Figure 1. Each map exhibits the propensity for strain localisation as a function of strain level according to the 8-bit colour scale shown for each strain mode.

cells exceeding a threshold magnitude that are in close proximity and act in a cooperative manner). The motivation for this study comes from the numerous cells present in the Rt maps that exhibit magnitudes that exceed the level at which critical strain localisation was predicted to occur by the Weibull analysis, yet no critical localisation was observed. As a result, the goal of this research is to determine (a) whether structure exists within the Rt data, and (b) the strength of any spatial correlations that may be present within this structure. (Note that quantification of spatial correlations in three dimensions presents a substantial challenge in itself, as

the available tools are designed for and, generally, limited to the analysis of two-dimensional data.) If the observable structure has no influence, then critical strain localisation is an uncorrelated stochastic process that can only be estimated through probability analyses. However, if structure is required, then where critical strain localisation occurs on the surface will depend on the local magnitudes of the surface heights as well as on the size, shape and density of that structure.

Two approaches were adopted to quantify the spatial correlations in the Rt data. The first is based on the conventional two-point autocorrelation function (ACF). The second is based on spectra derived from sets of complex eigenvalues that were calculated for the high-resolution topographies [17]. The second approach is similar to that employed in pattern recognition algorithms [18] and incorporates analysis concepts that are derived from information theory. The motivation for introducing information theory methods into the analysis of deformation-induced surface roughness is two-fold. First, given that plastic deformation is a volume conserving process, the topography of a deformed polycrystalline material contains substantial characteristic information regarding all of the physical mechanisms involved. Second, the relevant literature shows that information theory methods are rigorous, quantitative, flexible and minimally biased [19–24]. As a result, these methods are ideally suited to analyse large, complex data sets such as those produced by topographical analysis.

2. Experimental

2.1. Generation and evaluation of surface roughness

This section is a synopsis of the procedures presented in [11] that were used to generate surface data in the various strain conditions. Sets of 30×30 cm (12×12 in) blanks were sheared from 1-mm thick commercially available AA5754-O sheet stock for testing. This aluminium alloy was primarily developed for automotive applications and, like most alloys in the 5xxx series, AA5754 is substitutionally strengthened, and demonstrates good overall formability. Aluminium alloy AA5754 typically contains 2.8% mass fraction Mg for solid solution strengthening and approximately 0.5% mass fraction Mn for grain refinement and stability [25]. The grain structure was relatively equiaxed in the rolling plane and slightly elongated along the rolling direction of the sheet (RD), which is indicative of the recrystallised microstructure normally associated with the O-temper. The grain size for this alloy was 40 ± 20 μm [12]. All the specimens in this evaluation were polished to a 6 μm diamond finish using standard metallographic polishing practice to better reveal the surface character at low strains and to produce more consistent surface roughness measurements.

After polishing, the blanks were deformed in three in-plane, proportional strain modes defined in terms of the in-plane principal strain ratio $\rho = \varepsilon_2/\varepsilon_1$ [13]. The first strain ratio was $\rho = 1$ (hereafter referred to as equi-biaxial). The second strain ratio was $\rho = -0.5$ (hereafter referred to as uniaxial), and the third strain ratio was $\rho = 0$ (hereafter referred to as plane strain). The uniaxial samples were machined to an ASTM E08-91 standard sheet-type tensile specimen geometry and then strained to nominal true strain values of 5, 10 and 15% using standard test methods [26] with a

constant displacement rate resulting in an initial strain rate of $6 \times 10^{-4} \text{ s}^{-1}$. Both the equi-biaxial and plane strain deformations were imposed using an augmented [27] Marciniak flat bottom ram test [28]. Samples were strained in equi-biaxial tension using a typical strain rate of $5 \times 10^{-4} \text{ s}^{-1}$ to 5, 10, 15 and 20% nominal true strain. A third set of samples was strained to similar true strain levels in the plane strain condition. Additionally, one sample was taken to failure in each strain mode. Note for this investigation, ‘failure strain’ refers to the uniform strain measured after a localisation event occurred. Therefore, the surface roughness data acquired in this condition establish: (1) the maximum uniform surface roughness obtainable for the AA5754-O alloy in each strain mode, and (2) the surface conditions that gave rise to the formation of the failure event. Coupons were cut from the centre of each deformed specimen for topographic analysis.

The surface topography was quantified for each strain level in each strain mode with scanning laser confocal microscopy (SLCM). Note that the morphology within a localised region is specific to a unique set of surface conditions and no longer represents the character of the surface as a whole. In other words, due to the high degree of heterogeneity in the surface data in the proximity of a localised region, these data are non-stationary in a statistical sense. For this reason, neither the critical localisations, nor the regions immediately surrounding them, were included in any of the SLCM images acquired from the surfaces in the failure condition. Each measurement in this evaluation consisted of five, well-spaced SLCM images taken from different locations on the specimen surface. It was essential for these images to be well separated to ensure that the surface data contained in each image was statistically independent (i.e. no overlapping image data) and that the data properly represented the full range of surface characteristics. The SLCM images were converted from the image format to simple matrices of topographic data according to the procedure described in reference [29].

2.2. Generation of strain localisation maps

The relationship between surface roughness and strain localisation was quantified via the Rt roughness parameter. This parameter is formally defined as the vertical distance between the highest and the lowest points of a profile within a particular evaluation length [30]. That is,

$$Rt = Rp + Rv. \quad (1)$$

In this equation, Rp is the distance between the highest point of the profile and the mean line, and Rv is the distance between the lowest point of the profile and the mean line within a particular evaluation length. (Note that heights below the mean plane are traditionally considered negative). Constructing a Euclidean distance matrix based on this measure [31], extended the traditionally linear profile-based Rt parameter to a matrix format. Construction of this matrix required sub-dividing a 512-row \times 512-column source matrix (e.g. those shown in Figure 1) into smaller matrices each consisting of 16 elements (i.e. 4 heights/row \times 4 heights/column). The difference in the surface height for a given cell, $Rt_{(i,j)}$, was determined from the set of 16 height values contained in that cell. That is, each $Rt_{(i,j)}$ value represents the largest displacement

normal to the mean plane at the coordinates of the source with the matrix index (i, j) . The result is a differential matrix that contains 16,384 Rt values.

The maps in Figure 2 are examples of this construction. Note that both the magnitude and the physical location of each $Rt_{(i,j)}$ value are quantified by this method, since the matrix format retains the spatial coordinates for an Rt cell by construction. That is, this technique directly links any feature in the source image to the corresponding change in magnitude of the local surface height. Obviously, cell size has a strong influence on the information contained within the Rt map, and the level of resolution can easily be affected by a simple change in the dimensions of the sub-matrix cells. The cell size used in the previous evaluation was (8×8) . Decreasing the number total of elements in a cell from 64 to 16 increased the resolution of the Rt maps by a factor of four. The surfaces were re-evaluated at the higher resolution to differentiate between grain boundary roughening and within-grain roughening events. Assuming a uniform distribution of grains with an approximate area of $1600 \mu\text{m}^2$, the smaller $6.25 \times 6.25 \mu\text{m}$ cells would yield a minimum of 40 samples per grain. This sample density provided sufficient sensitivity to clearly discern the roughening that occurs within a grain (e.g. slip) and that located along the grain boundaries. Moreover, the improved resolution enabled a direct assessment of the topographical features produced by the plastic strains in each strain mode (Figure 1) and the corresponding change in the relative potential for critical strain localisation produced by those topographical features (Figure 2). Figures 1F and 2F were extracted, enlarged and presented as Figure 3A and B, respectively, to illustrate the good correlation between the surface topographies and the Rt maps.

Maps of the Rt data were constructed for the five surfaces acquired in each strain condition. As shown in Figure 2, the range of Rt magnitudes is mapped into a standard 8-bit colour scale, where blue is low and red is high, so that the colour of an individual cell reflects the local magnitude of Rt . From the previous findings, the maximum (the dark red cells online) in Figure 2 reflects a threshold Rt magnitude where the probability of a critical strain localisation event occurring is $\geq 95\%$ [11].

3. Analysis of Rt Data

As noted earlier, several cells were observed that exceeded the Rt magnitude predicted for the onset of critical strain localisation at strain levels where failure did not occur. This behaviour implies that the occurrence of an isolated, or single, Rt cell with a critical magnitude is not sufficient to produce failure. Further examination of the Rt maps for each strain condition (Figure 2) revealed that, as the strain level increases, some structure (i.e. clustering), or groups of cells with similar relative probabilities, appears to form in the Rt images. The sizes, locations, and densities of these Rt cell clusters also appear to vary with strain mode. It should be emphasised that in large part, this 'structure' is a consequence of the threshold values used for the upper and lower bounds of the colour scales in each map. However, it can also be linked to specific morphological features produced by the plastic deformation (Figure 3). Therefore, the presence of this structure raises the following question: Does the structure in the Rt maps play a significant role in the localisation, or is it merely an artefact arising from the methods used to construct and colour the Rt maps?

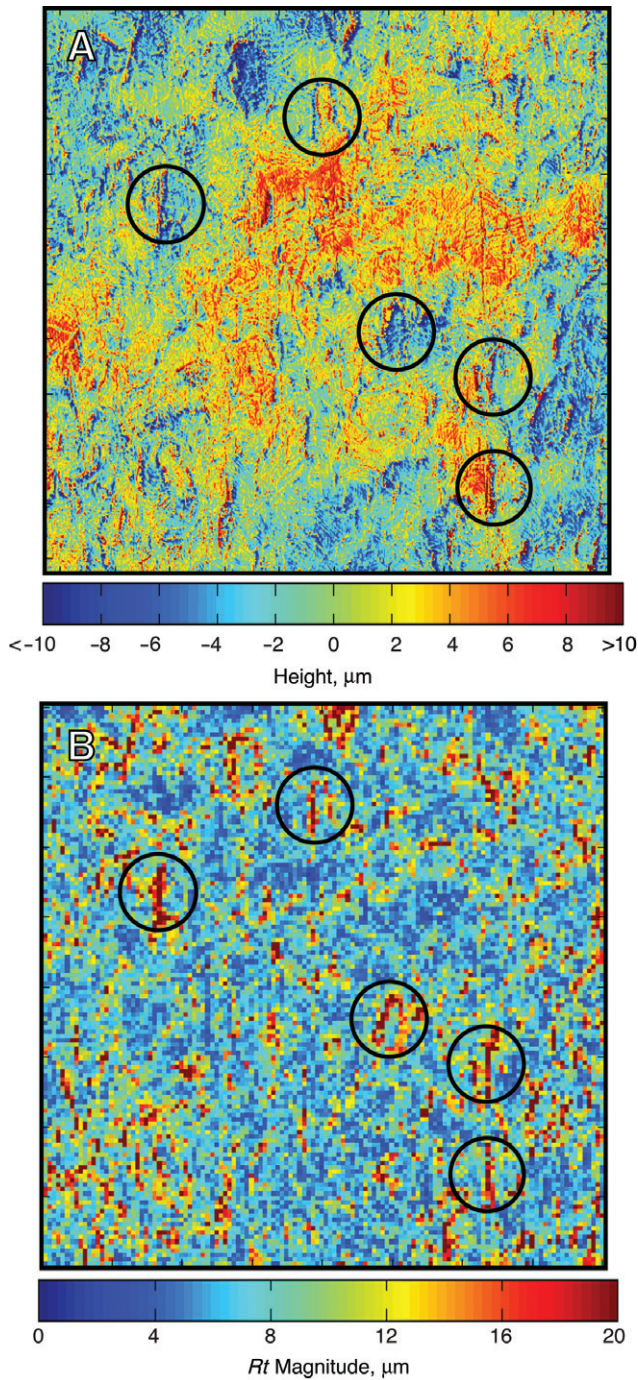


Figure 3. (Colour online). Figure 1F and Figure 2F enlarged and presented together to exhibit the correlation between the strain localisation (Rt map) and surface morphology. In addition, areas with a large number of cells that have localisation probabilities exceeding 95% and the corresponding locations on the topography have been isolated to illustrate the notion of clustering that may exist within the Rt maps.

3.1. Autocorrelation function approach

The auto-correlation function (ACF), defined as the correlation of a source with itself, is one of the more familiar techniques used to characterise the spatial arrangement in linear profile-based roughness data [30,32,33]. This technique can be easily extended to a three-dimensional form for evaluating the spatial characteristics of surface data [34]. The three-dimensional form of the ACF used for this analysis is derived from the cross correlation function for any $(m \times n)$ matrix, A , with itself [35]:

$$P(A_{(i,j)}) = \frac{\frac{1}{MN} \left| \sum_{m=0}^{M-1} \sum_{n=0}^{N-1} (A_{(m,n)} A_{(m+i,n+j)}) \right|}{Sq^2}. \quad (2)$$

In this equation, M and N are the dimensions of the matrix, Sq^2 is the square of the root mean squared roughness (i.e. the variance of the matrix), and the values in the ACF matrix, $\langle P(A_{(i,j)}) \rangle$, are the expectation values produced by lag (offset) vectors of a given magnitude, $|\tau_{(i,j)}| = \sqrt{(i^2 + j^2)}$, evaluated over the entire matrix. Since these values have been normalised, they range between (-1.0) and $(+1.0)$. Thus, the physical meaning of an individual ACF value is as follows: (a) a value of $(+1.0)$ indicates that the matrix is perfectly correlated at all values of the lag vector $\tau_{(i,j)}$; (b) a value of (0) indicates that there is no correlation at all values of the lag vector $\tau_{(i,j)}$ (i.e. random); (c) a value of (-1.0) indicates that the matrix is perfectly anti-correlated at all values of the lag vector $\tau_{(i,j)}$ (i.e. 180° out of phase) [33]. By construction, the ACF values returned by a lag vector with positive and negative values for (i,j) are identical, so the resulting ACF surfaces possess a quadrantal symmetry.

ACF surfaces were constructed for each Rt map using Equation (2) and the signal processing toolbox in MATLAB[®] [36]. The set of ACF surfaces derived from the Rt maps in Figure 2 are shown in Figure 4. Each plot in this figure depicts the magnitude of the ACF at any point in the Cartesian plane with each contour corresponding to a constant ACF value. Note that the Rt values used to construct these figures are all positive, so no anti-correlated regions are present in the ACF surfaces. Thus, the range of the corresponding 8-bit colour scale lies between $(0, \text{blue})$ and $(+1, \text{dark red})$ and is common to all the plots in the figure.

As shown by Brochard et al. [37], analyses of ACF surfaces can reveal a great deal of information pertaining to the spatial arrangement of the surface features. Unfortunately, the boundary conditions used in the ACF calculation have a strong influence on the results. For this reason, analyses of surface data with the ACF can be subjective and difficult to interpret. The most apparent feature in these plots is the area of high correlation, which appears as a diamond-shaped region distributed about the origin and extends more than $200 \mu\text{m}$ in both the x and y directions. Outside this central diamond region, the degree of correlation rapidly decays to zero. The correlation length, or the transition from the correlated to the random state, is the most common characteristic derived from the ACF and it is based on the decay of the ACF [32]. While this may be suitable to assess the characteristics of an ACF generated from a linear profile, extending this approach to three-dimensional data is not as straightforward, and does not readily produce meaningful results. Since the ACF data decay in more than one direction, the correlation length becomes a vector

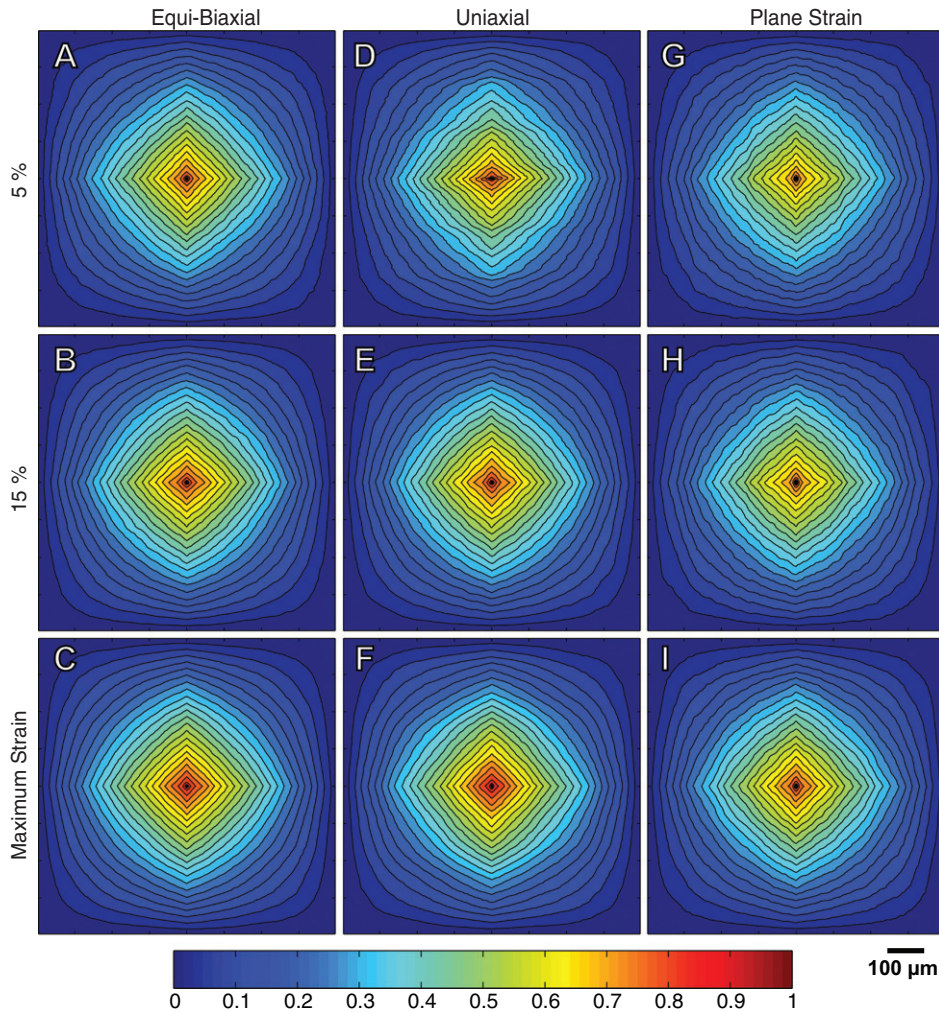


Figure 4. (Colour online). Two-point autocorrelation (ACF) surfaces constructed from Rt data sets shown in Figure 2. Each surface is a contour plot that reflects the magnitude of the ACF at any point in the Cartesian plane. Each contour line corresponds to a constant ACF value.

and must be determined with vector-based tools. One of the more common approaches is the fastest decay autocorrelation length, Sal [30]. This approach is normally used to generate a polar spectrum that can be used to assess the anisotropy of a surface [38]. While small differences are observable between the individual plots in Figure 4, the overall characters of the plots are strikingly similar to one another. This suggests that any differences are likely to occur at longer lag lengths where the statistical reliability may be severely degraded; thus, the fastest decay autocorrelation length is not the appropriate tool to evaluate the strength of the correlations in the Rt data. Methods that are more statistically robust, and exhibit better sensitivity to

Table 1. Analysis of the two-point autocorrelation function (ACF) data.

Strain path	Nominal true strain	ACF volume (μm^2)	Uncert. σ (μm_3)	ACF inertia (μm^2)	Uncert. σ (μm_3)
As-Polished	0.00	1.41E + 04	1.31E + 02	1.21E + 08	1.61E + 06
Equi-biaxial	0.05	1.32E + 04	2.13E + 02	1.15E + 08	1.89E + 06
–	0.10	1.33E + 04	1.31E + 02	1.17E + 08	1.47E + 06
–	0.15	1.35E + 04	9.75E + 01	1.18E + 08	9.95E + 05
–	0.20	1.34E + 04	9.44E + 01	1.17E + 08	9.44E + 05
–	0.26	1.40E + 04	1.74E + 02	1.22E + 08	1.23E + 06
Uniaxial (RD \perp)	0.05	1.35E + 04	2.46E + 02	1.19E + 08	1.96E + 06
–	0.10	1.33E + 04	3.36E + 02	1.17E + 08	2.22E + 06
–	0.15	1.26E + 04	1.69E + 02	1.10E + 08	1.94E + 06
–	0.23	1.32E + 04	3.90E + 02	1.15E + 08	3.05E + 06
Plane strain (RD \perp)	0.05	1.25E + 04	2.71E + 02	1.10E + 08	2.71E + 06
–	0.10	1.27E + 04	1.05E + 02	1.11E + 08	1.59E + 06
–	0.15	1.28E + 04	1.61E + 02	1.12E + 08	7.98E + 05
–	0.16	1.33E + 04	2.40E + 02	1.15E + 08	2.26E + 06

Note: ‘Uncert.’ refers to one standard deviation of the mean, σ .

correlations at long lag lengths must be employed to evaluate whatever differences may be present among the ACF surfaces. Two methods were adopted for this purpose.

The first method evaluated the overall volume of the ACF surface (i.e. the space enveloped by the ACF surface and the mean plane), which was estimated by a simple sum of all of the ACF magnitudes. Unlike the topographies, where the zero mean of the surface heights would produce a zero overall volume, the means of the individual *Rt* data sets were all non-zero and positive, producing ACF surface volumes that are also non-zero and positive. As shown in Table 1, the largest volume was observed in the as-polished data. This is not a surprising result in that little variation was observed in the overall surface structure for this particular condition, which produced large areas of similar height (i.e. high correlation). While the mean ACF volumes exhibit some variability in magnitude, the uncertainties associated with these variations indicate that the ACF volume data are relatively insensitive to strain level or to strain mode.

The second method employed to discriminate among the ACF surfaces was the moment of inertia. The quadrantal symmetry of the ACF surface allows for the construction of a centroid at the origin about which a moment of inertia can be calculated. The trace of the moment of inertia tensor [$I_{(i,j)}$] is a scalar quantity (*I*) that is determined from the sum of the products of the masses and the square of their distance from the axis of rotation [39]. In the case of an ACF surface, the ‘masses’ are taken to be the magnitudes of the ACF values at any given location in the ACF matrix $P_{(i,j)}$, and the distances are the matrix coordinates (*i,j*) of that ACF value. Thus, the moment of inertia for an (*n* × *n*) matrix is expressed as

$$I = \sum_{i=0}^n \sum_{j=0}^n (P_{(i,j)} R_{(i,j)}^2) \text{ where } R_{(i,j)}^2 = (i^2 + j^2). \tag{3}$$

The main advantage of this quantity over the ACF volume is that the moment of inertia is a measure that directly links the magnitude of an individual ACF value to the exact location in the Cartesian plane. Since the moment of inertia weights the values in the ACF as a function of their distance from the origin, it would seem to be a more proper metric to gauge the relative influences of the variations in the size of the diamond region and the small or near-zero values in Figure 4. However, as shown in Table 1, the moment of inertia data are similar to the ACF volume data in that they are relatively insensitive to changes in strain level or strain mode. The relative uncertainties associated with the ACF volume and moment of inertia estimates indicate that these quantities are credible measures of the strength of the spatial correlations present in the Rt data. Based on the relative magnitudes of the uncertainties shown in Table 1, the results of this analysis indicate that neither the strain level nor the strain mode produced statistically significant changes in the degree of correlation in the Rt data for this particular alloy.

3.2. Information theory approach

The spatial relationships within the Rt data were also analysed by constructing a set of normalised complex eigenvalues for all the Rt maps acquired in each strain condition. As shown in [17], the eigenvalue spectrum, $[\lambda_1, \lambda_2, \dots, \lambda_n]$, for a matrix A , i.e. $(\lambda(\frac{1}{\sqrt{n}}A))$ serves as a minimally biased ‘fingerprint’ that represents all of the magnitude information as well as all of the spatial correlations latent within A at all levels of complexity up to and including the rank of the matrix, n . In other words, the individual complex eigenvalue spectra directly reflect all of the deformation effects at a given strain condition for any Rt map. This deformation information is reduced to a set of n complex eigenvalues each containing both a magnitude and a phase component. Extracting the magnitudes and disregarding the phase information contained in the eigenvalue spectrum (i.e. setting each phase angle equal to zero) allows for the construction of a scalar quantity that distils the information regarding the magnitudes and the spatial correlations existing in the Rt matrix into a convenient form. This is accomplished by taking the absolute value of each eigenvalue, i.e. multiplying each eigenvalue by its complex conjugate and taking the square root: $|\lambda_i| = (\lambda_i \lambda_i^*)^{1/2}$.

Information theory allows one to compare the information contained in a given distribution with respect to some baseline, or reference state [20,21,24,40–47]. For this evaluation, a set of reference states was created by randomly permuting [48] all of the elements contained within each Rt matrix, thereby completely destroying all of the correlations in each matrix while preserving all of the characteristics of the original Rt distribution [49]. Since the first order statistical properties of each randomised Rt matrix are identical to those of the original Rt matrix, the eigenvalues of the randomised matrices reflect only the characteristics of the Rt magnitudes generated by the individual deformation conditions.

The eigenvalues for the five Rt matrices in each strain condition were combined to form a single ‘strip’ and then sorted in order of decreasing magnitude. The resulting superposition of eigenvalues represents the character of the entire surface in that strain condition. A similar superposition was constructed for the eigenvalues of

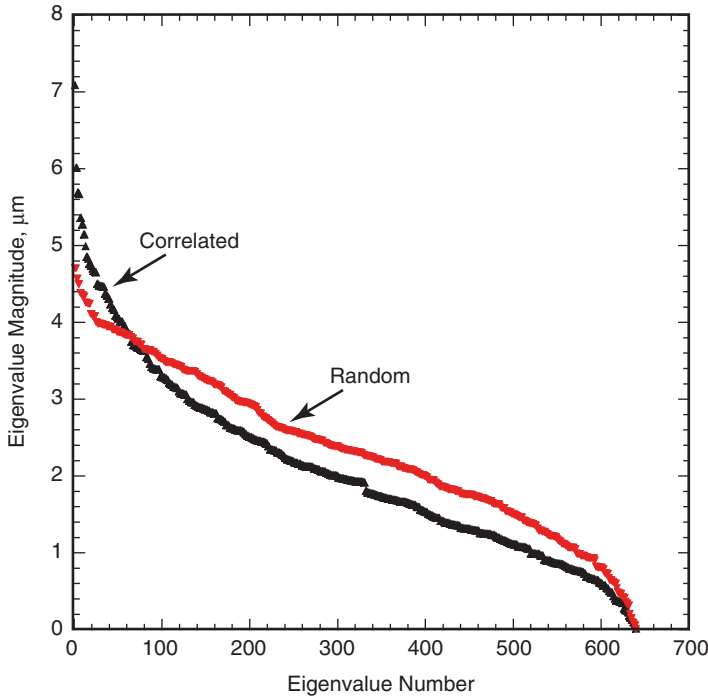


Figure 5. (Colour online). Two superposed eigenvalue distributions that represent the surface of AA5754-O at the maximum uniform strain condition in the uniaxial strain mode in two different conditions are shown. One contains the structural information (correlated) and the other has been permuted so that all of the structural information is destroyed (random).

the randomised matrices. An example of the differences between the superposed correlated and superposed random eigenvalue distributions is shown in Figure 5.

A pair of discrete probability measures, or ratios, was constructed from the eigenvalue distributions for each strain condition. One probability measure, $P(|\lambda_i|)$ (hereafter referred to as P), was based on the correlated eigenvalue distributions. A second, $Q(|\lambda_i|)$ (hereafter referred to as Q), was based on the random eigenvalue distributions. The probability measure, $A(|\lambda_i|)$, was defined in terms of the eigenvalue distribution (λ_i), the total number of eigenvalues (n), and the ratio associated with the i th eigenvalue magnitude as follows [17]²:

$$A(|\lambda_i|) = \left[\frac{|\lambda_i|}{\sum_{i=1}^n |\lambda_i|} \right], \quad \text{where } A = (P, Q). \tag{4}$$

The information content in A can be quantified directly by constructing another scalar measure known as the ‘spectral’ or Shannon entropy S_s . [41]. This spectral entropy is expressed as the negative of the expectation value of the logarithm of the probability measure, A :

$$S_s = - \sum_i A_i (\ln A_i) \quad \text{where } \sum_i A_i = 1. \tag{5}$$

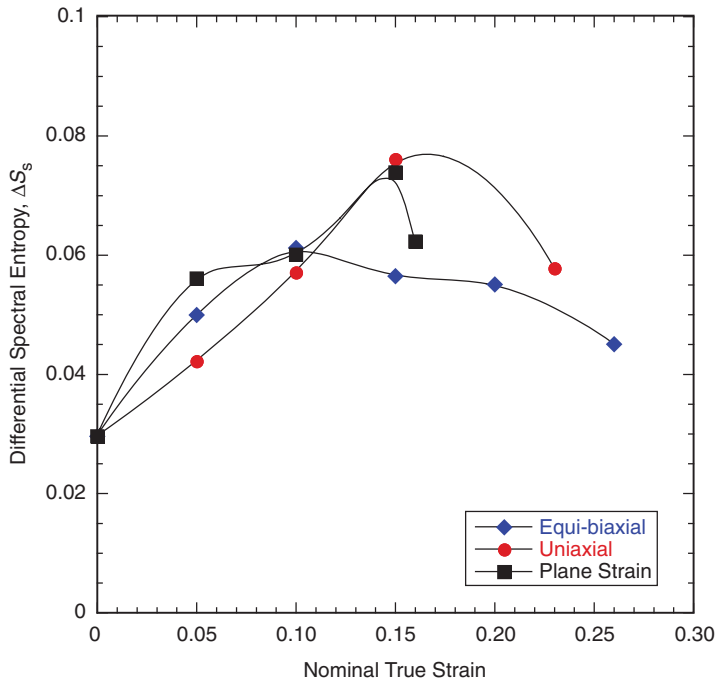


Figure 6. (Colour online). The differential spectral entropy, ΔS_s , is shown as a function of the nominal true strain and the strain mode. Note that ΔS_s is a dimensionless quantity.

The differential spectral entropy ΔS_s , or the global difference between the random and correlated conditions for a pair of eigenvalue distributions, defined as

$$\Delta S_s \equiv (S_s(Q) - S_s(P)) \quad (6)$$

is a measure of the complexity of the spatial correlations within a given Rt map. The differential spectral entropy is shown as a function of true strain and strain mode in Figure 6. In this figure, the ΔS_s behaviour for the uniaxial and plane strain modes are quite similar, showing a pronounced peak value at 15% nominal true strain followed by a sharp decrease to the failure strain. In contrast, the peak exhibited in the equi-biaxial mode is not as distinct as that shown in the other two modes and the spectral entropy decreases more slowly to failure.

If the two distributions have similar overall shapes, such as those shown in Figure 5, the differential spectral entropy may not have sufficient sensitivity to clearly distinguish the differences between the two. In this situation, one can define a ‘relative spectral entropy’, S_r , based on the Kullback–Leibler distance (KLD), which measures the ‘local’ discrepancy between any two pairs of probability distributions (P , Q) [40,46,50,51]. The symmetric form of the KLD has been adopted for this evaluation and is expressed as

$$S_r = \sum_i P_i \left(\ln \left(\frac{P_i}{Q_i} \right) \right) + \sum_i Q_i \left(\ln \left(\frac{Q_i}{P_i} \right) \right) \text{ where } \sum_i P_i = 1 \text{ and } \sum_i Q_i = 1. \quad (7)$$

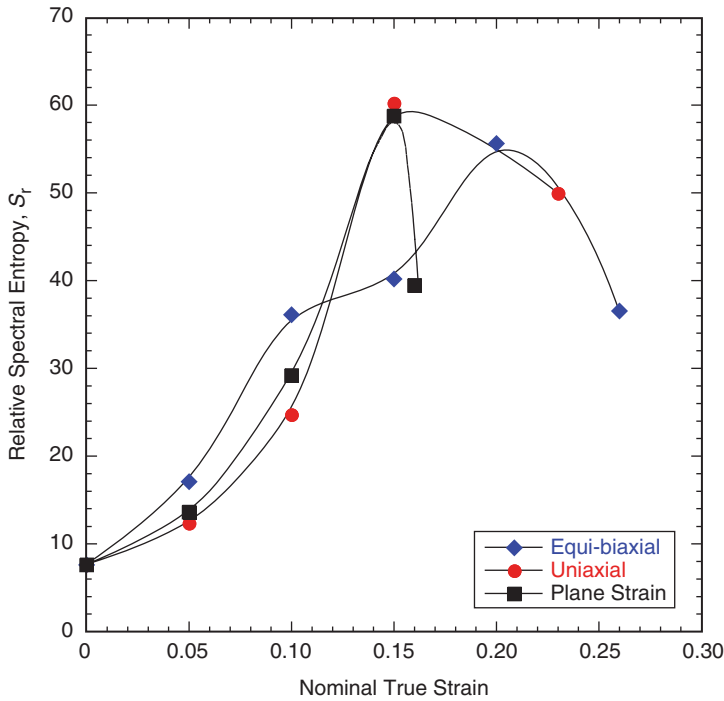


Figure 7. (Colour online). The relative spectral entropy, S_r , is shown as a function of the nominal true strain level and the strain mode. Note that S_r is a dimensionless quantity.

It should be noted that $S_r > 0$ for all cases except where $P_i = Q_i$ for all values of i . In this case, $S_r = 0$, which signifies that the two distributions are indeed identical. Even though the KLD is not a true metric or a physical ‘distance’ in a strict measurement sense, it can be regarded as an optimally sensitive discriminator between any pair of distributions, provided the two distributions are based on a common measure.

Relative spectral entropy data were plotted against the nominal true strain level and shown as Figure 7. The format for this figure is identical to Figure 6 enabling a direct comparison between the two entropies. Two trends are apparent. First, while only the uniaxial and plane strain modes exhibited similar shapes in Figure 6, the overall shapes of the curves in Figure 7 are more similar in that each strain mode exhibits a distinct peak that is immediately followed by a sharp decrease to the failure strain. This suggests that the decrease in relative spectral entropy might be a signature for the onset of critical localisation. Second, the magnitude ranges of the S_r data are considerably greater than the ΔS_S data for the same strain conditions. This amplitude increase indicates that the element-by-element comparison between the correlated and random distributions used in the relative spectral entropy calculation substantially enhances the signal-to-noise ratio in the Rt data compared to the differential spectral entropy, ΔS_S .

Figures 6 and 7 also illustrate how strain mode influences the general deformation behaviour of the aluminium sheet. That is, when presented as a

Table 2. Analysis of the divergence between individual surface measurements: Correlated.

Strain path	Nominal true strain	Mean K–L distance	Uncert. σ	Maximum K–L distance
As-polished	0.00	0.0097	0.0054	0.0173
Equi-biaxial	0.05	0.0073	0.0045	0.0135
–	0.10	0.0089	0.0064	0.0220
–	0.15	0.0142	0.0099	0.0347
–	0.20	0.0077	0.0043	0.0135
–	0.26	0.0077	0.0045	0.0142
Uniaxial (RD \perp)	0.05	0.0087	0.0055	0.0188
–	0.10	0.0104	0.0059	0.0182
–	0.15	0.0068	0.0042	0.0133
–	0.23	0.0099	0.0061	0.0178
Plane strain (RD \perp)	0.05	0.0054	0.0031	0.0091
–	0.10	0.0057	0.0033	0.0102
–	0.15	0.0089	0.0049	0.0156
–	0.16	0.0065	0.0042	0.0129

Note: ‘Uncert.’ refers to one standard deviation of the mean, σ .

function of the strain mode, the failure strain is considerably higher for the equi-biaxial mode compared to the uniaxial and plane strain modes. This is primarily due to the manner in which the macroscopic constant volume conditions are imposed by the individual strain mode during the deformation process [52]. Since the intent is to assess the entropy change as a function of strain intensity and strain mode, the results are all expressed in terms of a true strain in each strain mode. However, the entropy changes can also be expressed in terms of a normalised strain intensity, which can be calculated using the von Mises relationship for the effective uniaxial strain. Note if the entropy change is expressed in terms of the effective strain, the trends may not necessarily be the same as those shown in Figures 6 and 7.

The Kullback–Leibler distance [51] analysis can also provide a direct assessment of the statistical variability for the surface in general. This is accomplished by evaluating the KLD for each of the possible combinations of the five datasets according to the following:

$$KLD_{(M,N)} = \sum_i M_i \left(\ln \left(\frac{M_i}{N_i} \right) \right) + \sum_i N_i \left(\ln \left(\frac{N_i}{M_i} \right) \right) \text{ where } \sum_i M_i = 1 \text{ and } \sum_i N_i = 1. \quad (8)$$

In this equation, M and N represent the five data sets. Due to the form of the KLD adopted for this evaluation, this equation produces a 25-element symmetric matrix. A KLD analysis was performed on the data in each strain condition for both the correlated and randomised conditions. The KLD values are presented in Tables 2 and 3, respectively. Note that the magnitudes of the KLDs are relatively small and that the maximum KLD is approximately twice that of the mean value. This indicates that the five Rt maps for a given strain condition are remarkably similar in a general statistical sense.

Table 3. Analysis of the divergence between individual surface measurements: Random.

Strain path	Nominal true strain	Mean K–L distance	Uncert. σ	Maximum K–L distance
As-polished	0.00	0.0065	0.0037	0.0112
Equi-biaxial	0.05	0.0066	0.0037	0.0113
–	0.10	0.0057	0.0030	0.0089
–	0.15	0.0096	0.0068	0.0221
–	0.20	0.0094	0.0062	0.0191
–	0.26	0.0100	0.0064	0.0221
Uniaxial (RD \perp)	0.05	0.0075	0.0043	0.0127
–	0.10	0.0090	0.0053	0.0173
–	0.15	0.0055	0.0032	0.0093
–	0.23	0.0099	0.0065	0.0235
Plane strain (RD \wedge)	0.05	0.0090	0.0062	0.0213
–	0.10	0.0078	0.0057	0.0195
–	0.15	0.0086	0.0058	0.0176
–	0.16	0.0058	0.0045	0.0129

Note: ‘Uncert.’ refers to one standard deviation of the mean, σ .

4. Discussion of results

Throughout this evaluation, clusters have been referred to, but, in fact, the only statement resembling a definition of a cluster in this paper has been ‘*several Rt cells exceeding a threshold magnitude that are in close proximity and act in a cooperative manner*’. The rationale behind this is that defining a cluster in terms of a specific metric biases the analysis used to evaluate the spatial relationships that may, or may not, exist within a given dataset [53]. The definition of a cluster is not the only source of bias in these analyses. As noted previously, the colour scales used in Figures 2 and 3 are based on a 95% failure probability as predicted by a Weibull analysis. As a result, the 8-bit colour scales compress the tail regions of the Rt distributions to accentuate the areas of the Rt map where failure is most probable. Using this format to present the Rt data introduces a visual bias by artificially creating regions of cells with similar colour. However, the apparent structure that is present in these figures is simply an artefact introduced by the presentation. It is also possible to accentuate the segment of the Rt distribution that lies above the 95% probability level. Figure 8 exhibits how simply redefining the bounds of the 8-bit colour scale can influence the perception of clusters.

While it is impossible to conduct any analysis without introducing preconceptual bias in some form, the results of a spatial analysis are especially sensitive to the influence of such bias. Avoiding an *a priori* definition of a cluster (e.g. some predetermined shape consisting of n or more Rt elements, or n Rt elements in contact with one another in some arbitrary arrangement) and quantifying the multi-point spatial correlations directly produces a robust statistical analysis of any and all spatial relationships that are present, while simultaneously increasing the confidence in the assumption of independent conclusions drawn from that analysis.

The remarkable similarity between the ACF surfaces shown in Figure 4 and the ACF data in Table 1 demonstrates that the differences between the Rt maps are virtually indistinguishable at the two-point ACF level. One implication of this

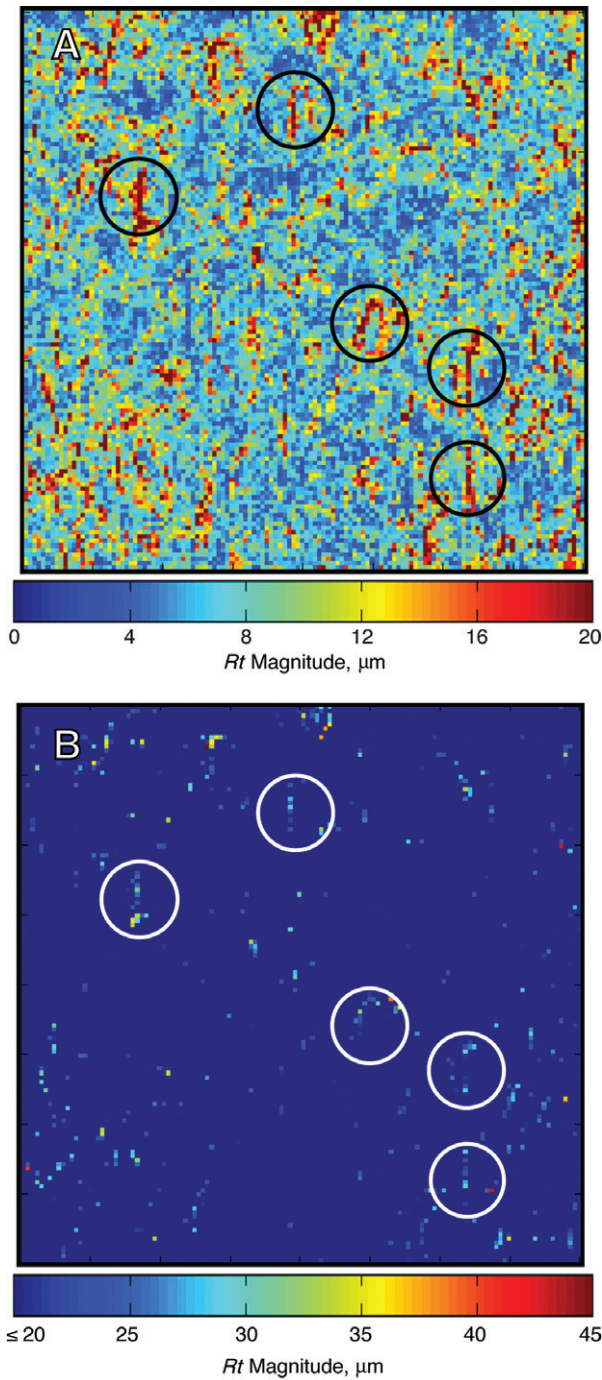


Figure 8. (Colour online). The influence of the colour scale on the perception of “clusters” that have formed within the Rt maps. Both maps present the Rt data shown in Figure 2F. A is shown using the original 8-bit colour scale (i.e. derived from the Weibull localisation probability analysis outlined in reference [11]), and B is shown using an 8-bit colour scale that has been recomputed to accentuate the range of probabilities that lie between the 95% and 99.9%.

statistical degeneracy is clear. The unexpected levels of similarity in the correlation results indicate that a two-point analysis lacks sufficient sensitivity to discriminate the complex spatial relationships that exist in the Rt maps. The presence of diamond-shaped regions of high-correlation in Figure 4 denote that correlations are indeed present within the Rt data; however, complex clustering, such as that exhibited in Figure 3, implies that these correlations are of a higher order and cannot be differentiated with a two-point analysis technique. While a two-point analysis may be entirely appropriate to assess the spatial relationships that exist within other datasets (such as those based on the measurement of a power spectrum), the ACF technique does not provide any reliable information that elucidates the nature of the relationship between complex clustering and the onset of critical strain localisation in the AA5754 alloy. This result also indicates that whatever influence the formation of Rt clusters may have on critical strain localisation can only be extracted with analytical methods that are based on multi-point spatial statistics [54].

The eigenvalue analysis is an attractive and powerful approach to quantify the existence of clusters within the Rt data for two important reasons. First, the complex eigenvalue spectrum calculated for each Rt map distils the spatial information present in that map into a compact scalar form. Second, it allows for the establishment of a well-defined reference state for comparison (e.g. the randomised condition). Analysis of the spatial relationships in the eigenvalue distributions by information theory-based methods, which offer high flexibility and minimal preconceptual bias by design, yields a systematic evaluation of any structure that may be present in any Rt map. Quantifying the comparative degrees of disorder (entropy) for two normalised distributions that correspond to a deformed surface in two different conditions (i.e. one that contains the correlation information, and one that does not) reveals the change in entropy produced by the formation of that structure. Both the spectral entropy and the relative spectral entropy are capable of quantifying this entropy change; however, the considerably higher signal-to-noise ratio in the relative spectral entropy results clearly indicates that this method is the more appropriate tool for this particular application.

The initial monotonic increase exhibited in each of the three relative spectral entropy curves shown in Figure 7 reflects the divergence of the correlated and random surface conditions at each strain level. Recall that all of the surface effects produced by plastic strain are directly reflected in the shape of the Rt distribution and that this distribution can be completely rearranged (randomised) with no change in the first-order statistical properties (i.e. mean, standard deviation, skew and kurtosis). This isolates the overall effects produced by an increase in plastic strain from the changes that occur in the surface structure generated by that increase. While it may appear relatively homogeneous on a macroscopic level, the deformation in a polycrystalline material occurs by highly complex and non-uniform processes. Each grain in a polycrystalline network deforms by different amounts as determined by the individual orientation of the grain, the local Schmid factor and the constraints imposed by neighbouring grains at or below the surface [55–57] and, for this reason, the local or grain level strain conditions have a strong influence on the overall character of the ensuing surface roughness. Increasing the level of plastic strain intensifies the crystallographic nature of the surface roughness and adds to the overall structure of the surface (see Figure 1). This increase in surface structure

results in a complementary change in the degree of disorder associated with the surface, and that is precisely what is exhibited in Figure 7.

Given that Rt is effectively the scalar projection of the height gradient, Rt maps such as those shown in Figure 2, serve as measures of the change in the local peak-to-valley height for a surface topography (Figure 1). However, the relationship between a topography and the corresponding Rt map is not necessarily isomorphic. Because it is derived from a set of surface height values, an Rt cell is a coarse-grained measure of the differential topography on a local level, which accentuates the microstructural features that promote critical strain localisation (e.g. cracks, splits and tears and necking). For example, consider a group of adjacent grains with orientations that do not favour primary slip. As the strain increases, these grains will rotate relative to one another in response to the applied strain and, in this situation, the deformation tends to concentrate in the grain boundary regions resulting in relatively large local displacements. This will produce a cluster of Rt cells that emphasises the displacement in the grain boundary regions rather than in the grain interiors. Therefore, the shape of this cluster is determined directly by the microstructure (Figure 3).

However, as shown in our previous analysis [11], the range of values (i.e. Rt magnitudes) in the distribution broadens markedly with increasing plastic strain, thereby augmenting and accentuating the tail region of the Rt distribution. This dispersion, caused by statistically rare events, makes it progressively less probable for similar Rt values to lie within close proximity of one another. In other words, since the range of potential Rt values expands with increasing plastic strain, it becomes increasingly more difficult to form groups of cells with similar Rt magnitude (clusters) as the strain level increases. This results in two competing processes: one where the formation of clusters is favourable and one where it is not. The maximum exhibited in the three curves in Figure 7 is produced by this competition. Both processes are dependent on changes in the surface morphology. At strains less than approximately 15% in the uniaxial and plane strain modes, and approximately 22% in the equi-biaxial mode, the first process, which primarily reflects the coalescence of Rt cells of similar magnitude, dominates the behaviour. At strains larger than these, the second process, which is more strongly influenced by rare probabilistic events that occur in the disproportionately long tail of the Rt distribution (such as the isolated cells present in Figure 8), dominates. Since the range of variability within the individual data sets for each strain condition, in both the randomised and correlated conditions is small, as shown in Tables 2 and 3, the maxima in Figure 7 cannot be an artefact caused by large statistical fluctuations in the surface data (i.e. the breakdown of stationarity). For this reason, the crossover can be considered a signature of the onset of critical strain localisation and, thus, a precursor to failure.

More explicitly, recalling that the data acquired in the failure condition establish the maximum obtainable surface roughness for the AA5754-O alloy as well as the morphological conditions that gave rise to the localisation event in each strain mode, the fact that exceptionally high Rt values were observed (Figure 8) and no failure occurred indicates that the surfaces in this condition are, in fact, metastable. It is, therefore, reasonable to hypothesise that the onset of metastability coincides with the occurrence of the maximum relative spectral entropy.

The results of these analyses prove that critical strain localisation requires the formation of structure within the Rt data. This structure cannot be distinguished by statistical methods that only describe correlations at the two-point level such as the autocorrelation function. While higher order correlation analysis clearly demonstrates that structure is present and that it is produced by the microstructure, the crossover from the process where the formation of clusters is favourable to the probabilistic process where it is not signifies the onset of critical strain localisation and failure. After this shift in the dominant process occurs, the surfaces become metastable and the application of additional strain produces perturbations that trigger the failure event. Because this process is more dependent on statistically rare events, predicting the exact location of that failure event with a deterministic model becomes significantly more difficult.

5. Conclusions

The spatial correlations present in surface data produced by three in-plane deformation modes (equi-biaxial, uniaxial and plane strain) were characterised with two different analytical approaches. The first was based on a conventional two-point autocorrelation function. The second was based on the complex eigenvalue spectra associated with each surface and information theory methods.

The data from the ACF approach were assessed by calculating the overall volume and the moment of inertia for each ACF surface. While the small uncertainties associated with the ACF volume and moment of inertia data confirmed that these quantities were statistically reliable measures of the spatial correlations, the results indicated that neither the strain level nor the strain mode produced a statistically significant change in the degree of correlation in the Rt data. Therefore, the conclusion drawn from the ACF analysis was that the ACF technique does not contain sufficient sensitivity to elucidate the nature of the relationship between complex clustering and critical strain localisation in the AA5754 alloy.

The data from the information theory-based approach revealed that quantifying the comparative degrees of disorder (i.e. information-theoretic entropy) for two normalised distributions that represent a deformed surface under two different conditions (one that contains the correlation information, and one that does not) directly reveals the change in the degree of disorder associated with the surface produced by the plastic strain. While both the spectral entropy and the relative spectral entropy are capable of revealing this change, the relative spectral entropy calculation was the more appropriate tool for this particular application. Each strain mode exhibited a monotonic increase in the relative spectral entropy as a function of true strain that attained a maximum, and then decreased sharply to the failure strain. This behaviour resulted from two competing processes: one where the formation of structure is favourable and one where it is not. The first process dominated the behaviour at strains up to and including the maximum S_r . At higher strains, the second process, driven by statistically rare events in the disproportionately long tail of the Rt distribution, dominated. Therefore, the crossover point can be considered as a precursor to failure because, once the dominant process shifts, additional strain results in the precipitate formation of a critical strain localisation event.

Notes

1. Certain commercial equipment, instruments, or materials are identified in this paper to foster understanding. Such identification does not imply recommendation or endorsement by the National Institute of Standards and Technology, nor does it imply that the materials or equipment identified are necessarily the best available for the purpose.
2. Note this measure is equivalent to a normalised eigenvalue distribution.

References

- [1] T. Foecke, M.A. Iadicola, A. Lin and S.W. Banovic, *Metall. Mater. Trans. A* 38 (2007) p.306.
- [2] F. Barlat, R.C. Becker, Y. Hayashida, Y. Maeda, M. Yanagawa, K. Chung, J.C. Brem, D.J. Lege, K. Matsui and S.J. Murtha, *Int. J. Plasticity* 13 (1997) p.385.
- [3] A.J. Beaudoin, A. Acharya, S.R. Chen, D.A. Korzekwa and M.G. Stout, *Acta Mater.* 48 (2000) p.3409.
- [4] D. Raabe, M. Sachtleber, H. Weiland, G. Scheele and Z. Zhao, *Acta Mater.* 51 (2003) p.1539.
- [5] R. Becker and O. Richmond, *Model. Simul. Mater. Sci. Eng. A* 2 (1994) p.439.
- [6] H.A. Al-Quershi, A.N. Klein and M.C. Fredel, *J. Mater. Proc. Tech.* 170 (2005) p.204.
- [7] J. Savoie, M. Jain, A.R. Carr, P.D. Wu, K.W. Neale, Y. Zhou and J.J. Jonas, *Mater. Sci. Eng. A* 257 (1998) p.128.
- [8] P.D. Wu, D.J. Lloyd, M. Jain, K.W. Neale and Y. Huang, *Int. J. Plasticity* 23 (2007) p.1084.
- [9] W.B. Liewers, A.K. Pilkey and D.J. Lloyd, *Acta Mater.* 52 (2004) p.3001.
- [10] J.E. Bird and J.L. Duncan, *Metall. Trans. A* 12 (1981) p.235.
- [11] M.R. Stoudt, J.B. Hubbard, M.A. Iadicola, S.W. Banovic, *Metall. Mater. Trans. A* 40 (2009) p.1611.
- [12] S.W. Banovic, M.A. Iadicola and T. Foecke, *Metall. Mater. Trans. A* 39 (2008) p.2246.
- [13] M.A. Iadicola, T. Foecke and S.W. Banovic, *Int. J. Plasticity* 24 (2008) p.2084.
- [14] H.J. Frost and M.F. Ashby, *Deformation-Mechanism Maps: The Plasticity and Creep of Metals and Ceramics*, Pergamon Press, Oxford, 1982.
- [15] G.W. Greenwood, *Mater. Sci. Eng. A* 410/411 (2005) p.12.
- [16] F.A. Mohamed and T.G. Langdon, *Metall. Trans.* 5 (1974) p.2339.
- [17] J.B. Hubbard, M.R. Stoudt and L.E. Levine, *J. Appl. Phys.* 102 (2007) p.1.
- [18] M. Turk and A. Pentland, *J. Cogn. Neurosci.* 3 (1991) p.71.
- [19] C. Arndt, *Information Measures Information and Its Description in Science and Engineering*, Springer, New York, 2001.
- [20] R.B. Ash, *Information Theory*, Dover, New York, 1990.
- [21] M.R. Fazlollah, *An Introduction to Information Theory*, Dover, New York, 1994.
- [22] R.M. Gray, *Entropy and Information Theory*, Springer, New York, 1990.
- [23] G. Jumarie, *Relative Information Theories and Applications*, Springer, New York, 1990.
- [24] A.I. Khinchin, *Mathematical Foundations of Information Theory*, Dover, New York, 1957.
- [25] Anon, *Aluminium Standards and Data 2003*, The Aluminium Association, Washington, DC, 2003.
- [26] Anon, in *1993 Annual Book of ASTM Standards, Section 3, Metals Test Methods and Analytical Procedures*, ASTM, Philadelphia, PA, 1993.
- [27] K.S. Raghavan, *Metall. Mater. Trans. A* 26 (1995) p.2075.
- [28] Z. Marciniak and K. Kuczynski, *Int. J. Mech. Sci.* 9 (1967) p.609.
- [29] M.R. Stoudt, J.B. Hubbard and S.A. Janet, *Mater. Sci. Tech.* 24 (2008) p.253.

- [30] Anon, *ASME Designation B46.1-2002: Surface Texture (Surface Roughness, Waviness, and Lay)*, The American Society of Mechanical Engineers, New York, 2002.
- [31] J. Dattorro, in *Convex Optimization and Euclidean Distance Geometry*, MeBoo Publishing, Palo Alto, CA, 2005.
- [32] T.R. Thomas, *Rough Surfaces*, Imperial College Press, London, 1999.
- [33] M.R. Stoudt and J.B. Hubbard, *Acta Mater.* 53 (2005) p.4293.
- [34] W.P. Dong, P.J. Sullivan and K.J. Stout, *Wear* 178 (1994) p.45.
- [35] S.J. Orfanidis, *Optimum Signal Processing*, Prentice-Hall, Englewood Cliffs, NJ, 1996.
- [36] Anon, *Matlab® R2007a*, The MathWorks, Inc, Natick, MA, 2007.
- [37] J. Brochard, M. Khoudeir and B. Augereau, *Pattern Recogn. Lett.* 22 (2001) p.759.
- [38] F. Blateyron, *New 3D Parameters and Filtration Techniques for Surface Metrology*, Quality Magazine (2006). Available at: www.qualitymag.com/.../New3DParametersandFiltrationTechniquesforSurfaceMetrology.pdf
- [39] D. Halliday and R. Resnick, *Physics*, Wiley, New York, 1978.
- [40] Anon. *Quantum Relative Entropy*, Wikipedia, The Free Encyclopedia, 2006. Available at: en.wikipedia.org/wiki/Quantum_relative_entropy
- [41] C.E. Shannon and W. Weaver, *The Mathematical Theory of Communication*, University of Illinois Press, Urbana, 1949.
- [42] P. Diaconis, *Bull. Am. Math. Soc.* 40 (2003) p.155.
- [43] A. Edelman, *J. Multivar. Anal.* 60 (1997) p.203.
- [44] S. Geman, *Ann. Prob.* 14 (1986) p.1318.
- [45] J. Ginibre, *J. Math. Phys.* 6 (1965) p.440.
- [46] S. Kullback, *Information Theory and Statistics*, Wiley, New York, 1959.
- [47] N. Lehmann and H.J. Sommers, *Phys. Rev. Lett.* 67 (1991) p.941.
- [48] G.J. Chaitin, *Sci. Am.* 259 (1988) p.80.
- [49] L.E. Levine, *A Permutation Algorithm for Randomizing the Elements within Square Matrices*, NIST, Gaithersburg, MD, 2006.
- [50] Anon., *Kullback–Leibler Divergence*, Wikipedia, The Free Encyclopedia (2006). Available at: en.wikipedia.org/wiki/Kullback-Leibler_divergence
- [51] S. Kullback and R.A. Leibler, *Ann. Math. Stat.* 22 (1951) p.79.
- [52] G.E. Dieter, *Mechanical Metallurgy*, McGraw-Hill, New York, 1986.
- [53] A. Kraskov, H. Stögbauer, R.G. Andrzejak and P. Grassberger, *Europhys. Lett.* 70 (2005) p.278.
- [54] B.D. Ripley, *Spatial Statistics*, Wiley-Interscience, Hoboken, NJ, 2004.
- [55] G.I. Taylor, *J. Inst. Metals* 62 (1938) p.307.
- [56] J.D. Eshelby, *Proc. R. Soc. Lond. A* 241 (1957) p.376.
- [57] M.F. Ashby, *Phil. Mag.* 21 (1970) p.399.